Results in Engineering 11 (2021) 100252

Contents lists available at ScienceDirect

Results in Engineering

journal homepage: www.sciencedirect.com/journal/results-in-engineering

Acoustic behaviour of 3D printed titanium perforated panels

Arun Arjunan *, Ahmad Baroutaji, Ahmad Latif

Centre for Engineering Innovation and Research, Additive Manufacturing of Functional Materials Research Group, University of Wolverhampton, Telford Innovation Campus, TF2 9NT, UK

ARTICLE INFO

Keywords:
Titanium alloy
Additive manufacturing
3D printing
Selective laser melting
Sound transmission
Sound absorption

ABSTRACT

Titanium alloys such as Ti6Al4V is amongst the most widely studied metallic materials in the broad context of metal 3D printing. Although the mechanical performances are well understood, the acoustic performance of 3D printed Ti6Al4V, and Ti6Al4V ELI (Extra Low Interstitial) has received limited attention in the literature. As such, this study investigates the normal incidence sound absorption coefficient (α) and Sound Transmission Loss (STL) of both Ti6Al4V and Ti6Al4V ELI samples manufactured using Selective Laser Melting (SLM). The influence of material thickness on acoustic responses and the potential of developing Ti6Al4V micro-perforated panels (MPP) at 400–1600 Hz is also explored. The sound absorption of three aesthetic perforations printed using Ti6Al4V and the influence of a porous back layer was also investigated. The experimental measurements were carried out using an impedance tube following ISO10534-2. The result of the study establishes that 3D printed non-circular perforations featuring porous back-layer can exhibit improved sound absorption coefficient.

1. Introduction

Structures featuring high mechanical properties, energy absorption and acoustic performance are of interest to numerous sectors such as automotive, aerospace and the built environment [1–3]. Automotive floor panels [4] and aerospace bulkheads [5,6] are examples of mechanical structures where the secondary function extends to vibro-acoustic isolation [7,8]. Metallic foams [9] have gained popularity as a potential contender in this aspect due to their sound absorption coefficient. However, metallic foams still cannot match the structural performance of their bulk counterparts. As such, there is a requirement for alternative sound absorbers that feature good acoustic properties while offering excellent structural integrity.

Maa [10,11] proposed a design based sound-absorbing technology called Micro-Perforated Panel (MPP) that may be modified to suit these situations. The MPPs originally put forwarded by Maa used minute holes of radius r over a panel of thickness d at a perforation ratio φ resulting in an acoustic impedance Z. If the acoustic impedance of the panel (Z) can be matched to the air impedance (Z_0), then the MPP can provide significant sound absorption coefficient (α) [12,13]. However, doing this requires an imaginary impedance that counteracts the reactive part of Z, which can be introduced by an air cavity of depth L. The result of the coupled structure is a single-layer MPP whose performance depends on the variables r, d, φ and L.

Building on Maa's model, Kang and Fuchs [14] later introduced the influence of plate vibrations. Various other designs such as multiple panels were also experimented with to improve the sound transmission loss (STL) [15,16]. Notable modifications include the one proposed by Cobo et al. [17–19] where MPPs were used in conjunction with active control to form hybrid systems resulting in wideband α. Generally, a broadband (100–3150 Hz) high α MPP require thousands of microscopic perforations per square metre where the fabrication becomes challenging. This has led to several studies [20–22] focusing on strategies for reducing the manufacturing costs of MPPs leading to the introduction of slits known as micro-slotted panels (MSPs) [23–25]. Combining traditional MPPs with micrometric mesh resulting in a micro-perforated insertion unit (MIU) [26] are other notable modifications. MIUs offer the advantage of the carrying plate which can be machined and micrometric meshes can be introduced as separate elements which help to reduce the cost [27].

Honeycomb sandwich back-cavity MPP by Meng et al. [28] and the parallel-arranged sub-cavity by Min and Guo [29] are other potential directions. These approaches show that the design of the back cavity can influence peak absorption frequency which was also confirmed by Miasa et al. [30] through extensive studies on partitioned MPPs. This study also showed that varying the perforation dimensions widens the

* Corresponding author. School of Engineering, Faculty of Science and Engineering, University of Wolverhampton, Telford Innovation Campus, Telford, TF2 9NT, UK.

E-mail address: a.arjunan@wlv.ac.uk (A. Arjunan).

https://doi.org/10.1016/j.rineng.2021.100252
Received 26 June 2021; Received in revised form 16 July 2021; Accepted 17 July 2021
Available online 21 July 2021

absorption frequency bands compared to traditional MPPs. While the literature discussed thus far utilises impedance models and methods to study the acoustic performance of various MPP systems [31–34], no studies have been devoted to the acoustic performance of alternatively shaped perforations (non-circular) on metal MPPs. One of the primary reasons for this is the difficulty in manufacturing such microporous architecture at a low cost. This meant that aesthetic perforations cannot be translated to acoustic advantage simply because design data is unavailable. Furthermore, neither α nor STL of additively manufactured Titanium alloys is available in the literature. Moreover, the application of a porous back-layer on metal MPPs is another dimension of investigation that offers the potential to develop a structurally strong and compact acoustic system suitable for practical application.

The rise of 3D printing techniques such as selective laser melting (SLM) [35,36] can create complex perforations that are geometrically accurate and repeatable [37–39]. Although outside of MPP, Zhang et al. [40] developed continuously graded 'phononic' crystals using SLM and showed a broadband noise reduction potential at 1.35–3 kHz. The potential for carefully controlled geometrical architecture was also by Gao and Hou [41] in addition to Aslan and Turan [42] in achieving enhanced acoustic performance. In general, the geometrical freedom offered by 3D printing is accelerating the developments in design-based materials [43–45]. The rise in metamaterials targeted towards acoustic [46,47], energy harvesting [48] and auxetic [49,50] performance are all examples of the effectiveness of additive manufacturing in conceiving intricate geometric architecture.

Overall, there are various directions in which the research community is expediting design-based acoustic solutions. Nevertheless, the literature on α and STL performance regarding AM metal MPPs are scarce. In any case, studies on the acoustic behaviour of non-circular perforations except for slits are yet to be investigated. In this regard, this study explores the potential of developing a 3D printed Ti6Al4V non-circular MPP system focusing on both α and STL. The fabrication is realised by taking advantage of the SLM 3D printing process in Ti6Al4V. Emphasis was placed on the perforation shape effective at 400–1600 Hz.

According to Maa [3], for optimum sound absorption, the ratio of hole diameter to the thickness of the MPP should be one. This means that for a practical MPP sound absorber the thickness of the panel will be sub-millimetres resulting in significant structural challenges during installation and maintenance. Furthermore, the MPP will be purely for acoustical reasons and cannot be expected to contribute towards the structural integrity of the overall system requiring additional load-bearing components. As such, this research investigates structurally robust MPPs that can be 3D printed in Ti6Al4V for aerospace and motorsport applications. Building on the methodology proposed by Maa, strategies to improve α using a porous back layer is explored so that the thickness of the MPP can be designed to preserve the structural stability of the overall system. Furthermore, the use of non-circular perforations taking advantage of the design freedom offered by the 3D printing process to exploit the hole interaction effects is also investigated [51].

2. Material and methods

2.1. Non-circular micro-perforated panels (MPPs)

Porous rigid frames are characterised by their porosity and flow resistivity, which is, related to the size of the perforation and the perforation rate [52]. Therefore, approximating an MPP as a porous frame, the acoustic effect can be attributed to the perforation rate or porosity (φ), perforation size or flow resistivity (σ), perforation thickness (d) and the mounting conditions. Even though the panel vibration also plays a role, for most cases the stiffness can be neglected and only inertia need to be accounted for. Depending on the design, the base material can also affect the acoustic performance of MPPs, as a result, non-metallic materials are often used resulting in poor structural strength. In such cases, MPPs combined with a suitable backing cavity and additional porous layers forms an effective design [14,53].

Rather than using the traditional methodology [10,21,54], this study presents a general methodology that can handle aesthetical perforation using a transfer function method [52]. It is shown that the peak frequency of a random shaped MPP can be characterised using an equivalent fluid model following the Johnson–Allard approach. The methodology adopted follows the work of Atalla and Sgard [52] where it was shown that classical models for MPPs can be reobtained using the equivalent fluid model.

For an MPP backed by an air cavity of depth L, the air in the cavity can be considered partitioned at normal incidence. This means that the MPP can be approximated as a collection of Helmholtz resonators [55–58]. Here each cell represents an individual Helmholtz resonator with an air cavity volume V_{cav}, neck length d and neck aperture area A_{perf}, the volume in this instance, can be linked to the back-cavity depth L using Eqn. (1):

$$V_{cav} = \frac{A_{perf} \times L}{\varphi} \tag{1}$$

However, since the acoustic wavelengths under consideration are larger than the cavity dimensions, the normal surface impedance of the air layer can be expressed as shown in Eqn. (2):

$$Z_B = -j\rho_0 c_0 \cot(k_0 L) \tag{2}$$

where $\rho_0 = 1.225\ kg/m^3$ is the density of air, $c_0 = 343\ m/s$ is the sonic velocity and $k_0 = \omega/c_0$ is the wavenumber. Accordingly, the total input impedance of the perforated-air layer combination can be written as shown in Eqn. (3):

$$Z_A = \left(\frac{2d}{r} + 4\frac{\varepsilon_e}{r}\right)\frac{R_s}{\varphi} + \frac{1}{\varphi}(2\varepsilon_e + d)j\omega\rho_0 - j\rho_0 c_0 \cot(k_0 L) \tag{3}$$

It can be seen that Ingard [59] in calculating the resistive part of the impedance in the perforation assumed a different correction length than the one used for the inertial part. This can be associated with the assumption that the distorted flow area may span half a sphere of radius r centred at the surface of the perforation. It is well known that for such a resonance-based system the highest α corresponds to the frequency of maximum resonance, which in this case occurs at zero reactance. Therefore, following Atalla and Sgard [52], the first mode of resonance at low frequency can be written as shown in Eqn. (4):

$$\omega = \sqrt{\frac{c_0^2 \varphi}{(2\varepsilon_e + d)L}} \tag{4}$$

Equating Eqn. (4) with Eqn. (1), the resonant frequency (ω) can be expressed in terms of the perforation area (A_{perf}) as shown in Eqn. (5):

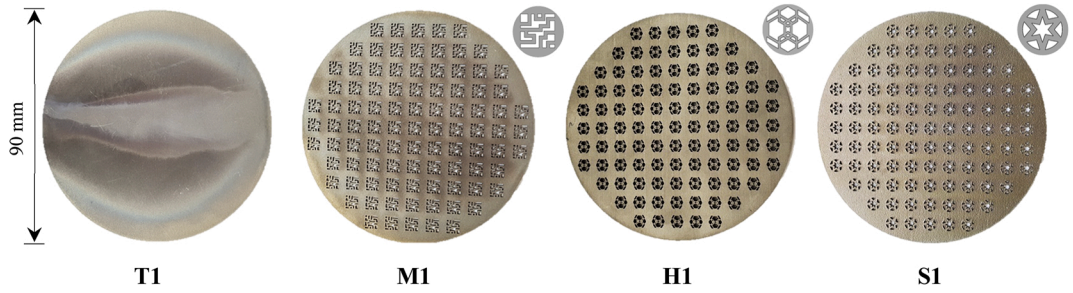

Fig. 1. Design variants considered for a 1 mm Ti6Al4V MPP showing identifiers for solid (T1), maze (M1), hexagonal (H1) and star (S1) design.

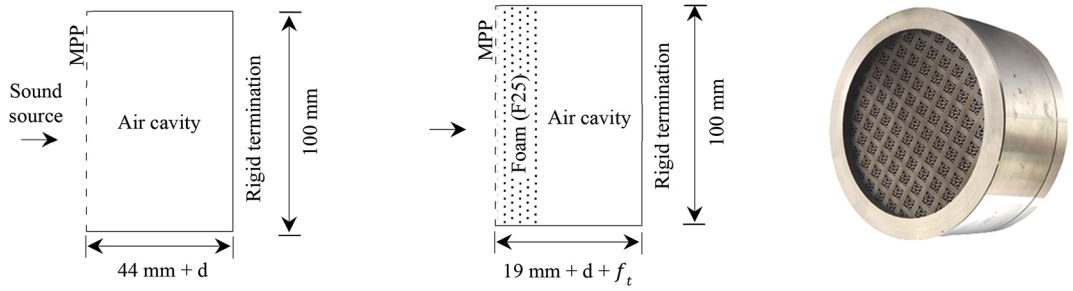

Fig. 2. Test cases considered where (a) MPP backed by 44 mm air cavity, (b) MPP backed by 25 mm foam and 19 mm air cavity and (c) MPP holder and test assembly used.

$$\omega = \sqrt{\frac{{c_0}^2 A_{perf}}{(2\varepsilon_e + d)V_{cav}}} \tag{5}$$

where A_{perf}/V_{cav} represents the ratio of the perforation area to the corresponding volume of the backing cavity and $\varepsilon_e \approx \varepsilon_0(1 - 1.14\sqrt{\varphi})$ is the correction term accounting for the interaction between the perforation. d is the perforation thickness and $c_0 = 343\, m/s$ is the sonic velocity. Furthermore, ε_0 can be related to A_{perf} assuming the radiation reactance of a circular plane piston baffled in an infinite wall as shown in Eqn. (6):

$$\varepsilon_0 \approx \frac{8}{3\pi}\sqrt{\frac{A_{perf}}{\pi}} \tag{6}$$

This shows that the resonance frequency of the corresponding MPP based on the equivalent fluid model can be classified using the perforation area, which is the design strategy considered. Accordingly, keeping the $A_{perf} \approx 2.54 \times 10^{-6}\, m^2$ (equivalent area of a circle of diameter 1.8 mm) as a constant, three different perforation shapes (M1, H1 and S1) were designed as shown in Fig. 1. However, the ratio of the small to large area (A_s/A_l) within a perforation is 0.6, 0.3 and 0.15 for S1, M1 and H1 respectively. An additional design T1 was also conceived and made of fully dense Ti6Al4V. This was used as the control specimen to characterise the acoustic performance of the AM material. The thickness (d) and diameter (D) of the panel used is 1 and 90 mm, respectively.

For the perforated designs (M1, H1, and S1), two test cases were considered: case 1 with (Fig. 2a) and case 2 without (Fig. 2b) a porous foam backing. To minimise air gaps and to ensure repeatability, the assemblies are made inside a holder as shown in Fig. 2c. The thickness of foam (f_t) used was 25 mm. A summary of the properties and the test designs are listed in Table 1.

Table 1
Properties of the designs and materials considered.

Design	Thickness (mm)	Foam placement	A_{perf} (10^{-6} m^2)	A_s/A_l	L (mm)
T1	1	–	–	–	44
F25	25	–	–	–	20
S1, M1, H1	1	–	2.54	0.6_{S1}, 0.3_{M1}, 0.15_{H1}	44
S1F25, M1F25, H1F25	$1_{MPP}+25_{foam}$	Rear	2.54	0.6_{S1}, 0.3_{M1}, 0.15_{H1}	19

The flow resistivity of the perforated panel is 7312 Pa s/m^2 and foam is 10,900 Pa s/$m.^2$.
The tortuosity of the foam is 1.

2.2. 3D printing

All the MPPs were 3D printed using an EOS M290 machine at 30 μm layer thickness. This is a laser powder bed fusion (L-PBF) system featuring a 400-W fibre laser and a build volume of 250 × 250 × 325

Table 2
Chemical composition of the material used.

Material	Al	V	C	Fe	O	N	H	Ti
Ti6Al4V ELI	5.5–6.5	3.5–4.5	<0.08	<0.25	<0.13	<0.05	<0.012	Bal.
Ti6Al4V	5.5–6.7	3.5–4.5	–	–	–	–	–	Bal.

mm. Atomised Ti6Al4V and Ti6Al4V ELI with a bulk density of 4430 kg/m^3 were used as the powder bed feedstock. Extra-low interstitials refer to the reduced levels of oxygen, nitrogen, carbon, and iron present in the composition. Although both Ti6Al4V and the ELI variant offers high strength, low weight ratio and outstanding corrosion resistance. The lower interstitials result in improved ductility and better fracture toughness which makes them desirable for a range of applications [60,61]. Ti6Al4V ELI is stabilised as a mixture of BCC (β) and HCP (α) phases resulting in Yield strength ranging from 930 to 795 MPa [62,63].

The feedstock featured a 10–45 μm particle size at a D50 of 27 μm. Titanium alloy was used due to its high stiffness, strength and low weight making it suitable for aerospace and motorsport applications. The composition of the material is summarised in Table 2. The selective laser melting was carried out at a laser power of 175 W at a scan speed of 1250 mm/s resulting in a fully dense print. All samples were built flat on the base plate using solid support structures which were removed using wire EDM. The printed samples were cleaned using compressed air, grit blasted and heat-treated in argon for 3 h at 650 °C.

2.3. Acoustic testing

2.3.1. Sound absorption coefficient (α)

The sound absorption coefficient (α) was measured using the impedance tube setup following ISO10534-2 [64] at a relative humidity and temperature of 64 % and 20 °C respectively. The acoustic source was an in-tube generator externally connected to a frequency controller. The sound pressure level (SPL) generated within the impedance tube post-excitation was recorded via high sensitivity microphones. The first (m_1) and second (m_2) microphones were placed at 150 mm and 230 mm from the test specimen. Based on the acoustic pressure levels p_1 and p_2 from microphones m_1 and m_2 respectively, the transfer function H_{12} and normal incident sound reflection factor r was computed using Eqs. (7) and (8):

$$H_{12} = \frac{P_2}{P_1} \tag{7}$$

$$r = r_r + jr_i = \frac{H_{12} - e^{-j\,ks}}{e^{j\,ks} - H_{12}} e^{2jkx_1} \tag{8}$$

where P_1 and P_2 are the transformed pressure level from p_1 and p_2. The parameters r_r and r_i represents the '*real*' and '*imaginary*' parts of the acoustic reflection. The distance between the two microphones is s and x_1 is the length from the sample to m_2. Furthermore, $k = 2\pi f/c$, at a sonic velocity of c and frequency f. As such α of the samples being tested can be calculated using Eq. (9):

$$\alpha = 1 - |r|^2 \tag{9}$$

For repeatable measurements, an airtight mount and rubber sealant ring was used to fit the specimen to ensure no sound leakage as shown in Fig. 3. These elements were kept constants for all samples to not influence the acoustic measurements. Each sample was analysed at 1/3rd octaves at $k = 1/3$ where the step size was represented using Eq. (10):

Fig. 3. 3D printed titanium MPP mounted in the impedance tube.

$$\frac{f_{n+1}}{f_n} = 2^k \tag{10}$$

2.3.2. Sound transmission loss (STL)

STL was characterised using a 4-microphone rig that was arranged as shown in Fig. 4. The arrangement featured two additional microphones m_3 and m_4 that were placed in the closed terminal. While the microphones in the source chamber capture the incident acoustic pressure the transmitted pressure was measured at the other end. As such the sound pressure at the respective microphones were computed using Eq. 11–14: where x_1, x_2, x_3, and x_4 are the length at which the respective microphones m_1, m_2, m_3 and m_4 are placed, respectively. A and B represent the incident and the reflected sound in the first chamber whereas C and D refer to the transmitted and the reflected sound in the 2nd chamber as shown in Eq. 15–18:

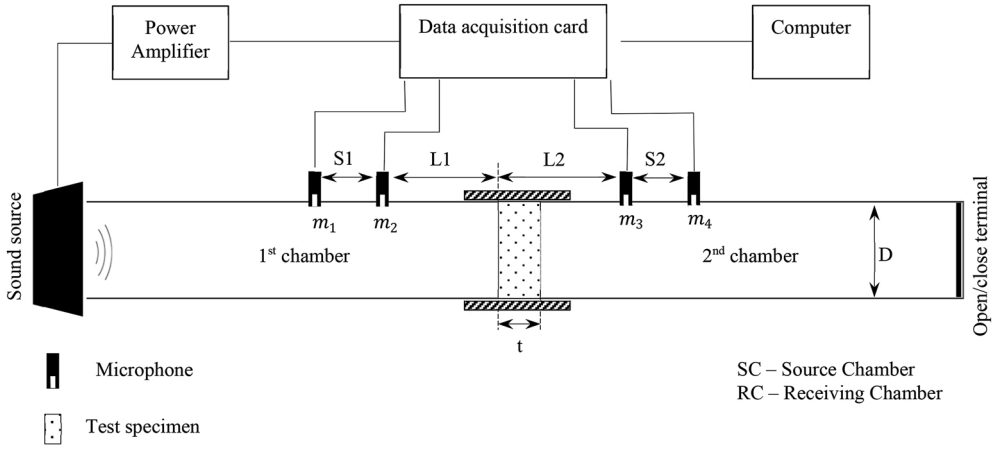

Fig. 4. Test right used to characterise the STL of the 3D printed samples.

$$P_1 = \left(Ae^{-jkx_1} + Be^{jkx_1}\right)e^{j\omega t} \tag{11}$$

$$P_2 = \left(Ae^{jkx_2} + Be^{-jkx_2}\right)e^{j\omega t} \tag{12}$$

$$P_3 = \left(Ae^{-jkx_3} + Be^{jkx_3}\right)e^{j\omega t} \tag{13}$$

$$P_4 = \left(Ae^{jkx_4} + Be^{-jkx_4}\right)e^{j\omega t} \tag{14}$$

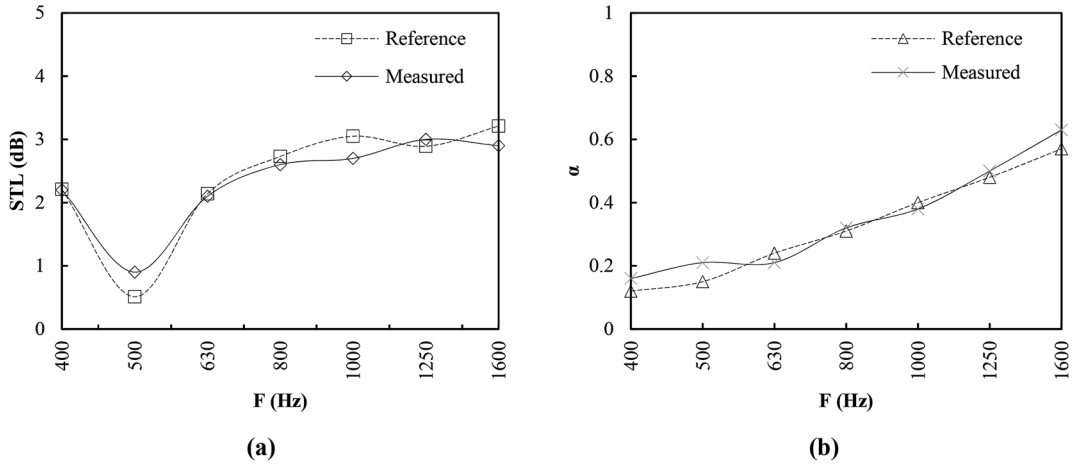

(a) (b)

Fig. 5. Validation of the experimental test setup showing the difference between actual and measured data for (a) sound transmission loss and (b) sound absorption.

Table 3
Comparison of allowable measurement uncertainty against measured for sound transmission loss.

Frequency (Hz)	Measurement Uncertainty	
	Acceptable (±dB)	Measured (dB)
400	1.2	+0.01
500	1.2	- 0.39
630	1.2	+0.04
800	1.0	+0.13
1000	1.0	+0.35
1250	1.0	- 0.11
1600	1.0	+0.31

$$A = \frac{j(P_1 e^{jkx_1} - P_2 e^{jkx_1}}{2\sin k\,(x_1 - x_2)} \tag{15}$$

$$B = \frac{j(P_2 e^{-jkx_1} - P_1 e^{-jkx_2}}{2\sin k\,(x_1 - x_2)} \tag{16}$$

$$C = \frac{j(P_3 e^{jkx_4} - P_4 e^{jkx_3}}{2\sin k\,(x_3 - x_4)} \tag{17}$$

$$D = \frac{j(P_4 e^{-jkx_3} - P_3 e^{-jkx_4}}{2\sin k\,(x_3 - x_4)} \tag{18}$$

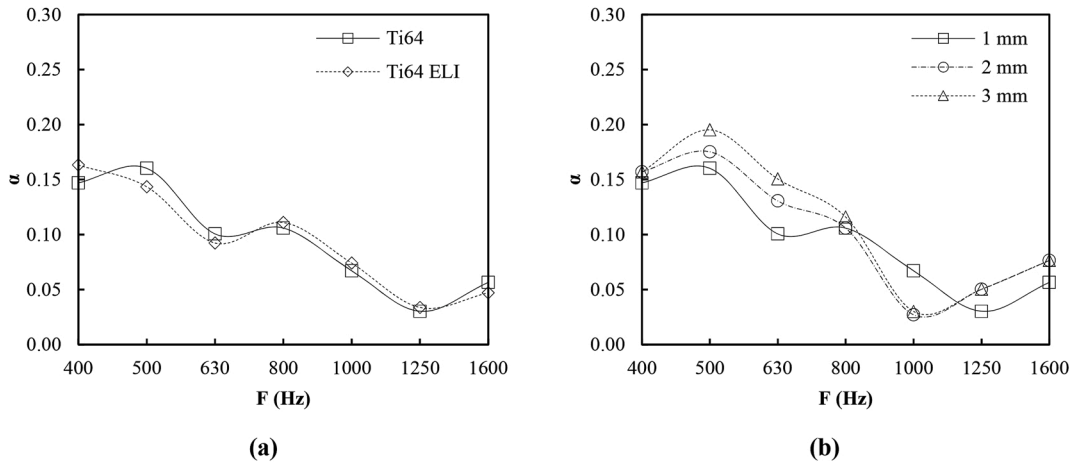

Fig. 6. Normal incident sound absorption coefficient measured for (a) 1 mm Ti6Al4V and Ti6Al4V ELI unpolished flat specimens manufactured using SLM and (b) showing the influence of material thickness.

The data was collected for two scenarios; with 2nd chamber closed (subscript 1) and open (subscript 2) which were compiled using Eq. (19) to solve for α:

$$\alpha = \frac{A_1 D_2 - A_2 D_1}{C_1 D_2 - C_2 D_1} \tag{19}$$

where A_1, C_1, D_1 and A_2, C_2, D_2 are the pressure levels captured at the two chambers. As such the STL matrix brings together the forward and backward travelling components as listed in Eq. (20):

$$\begin{Bmatrix} A \\ B \end{Bmatrix} = \begin{bmatrix} \alpha & \beta \\ \gamma & \delta \end{bmatrix} \tag{20}$$

where α and δ are the pressure transmission loss coefficient of test specimen determined from the first chamber and receiving chamber, respectively. β and γ are the acoustic impedance parameters of the waveguide. Subsequently, the STL can be computed using Eq. (21):

$$STL = -20\log(\alpha) \tag{21}$$

3. Results and discussion

3.1. Validation

When using impedance tube experimental setup, it is important to calibrate and validate the setup before commencing the characterisation of the 3D printed test samples. This is often done by measuring acoustic data of a material where the performance from an alternate laboratory is available for comparison. This step not only validates the test setup compliance with ISO10534-2 [65] but also quantified the measurement accuracy. A polymeric foam material with a density of 6 kg/m^3 at a 25 mm thickness was used as the reference material for the test rig validation.

The acoustic qualifiers describing the sound performance of any material is its experimentally measured α and STL. As such the reference material was characterised for both parameters to quantify the measurement uncertainty. The sound transmission is characterised in decibels and the higher the value the higher is the sound insulation. However, α is the ratio measured from 0 to 1, where 0 indicates no sound absorption and 1 indicates complete absorption. Comparison of the measured values with respect to reference data obtained from an independent test at a one-third octave band is shown in Fig. 5. A comparison of the curves as shown in Fig. 5a and b shows a good agreement between the actual and measured data for both α and STL, respectively. As listed in Table 3, the maximum change was 0.39 dB at 500 Hz which is well within acceptable measurement uncertainty following BSENISO10140

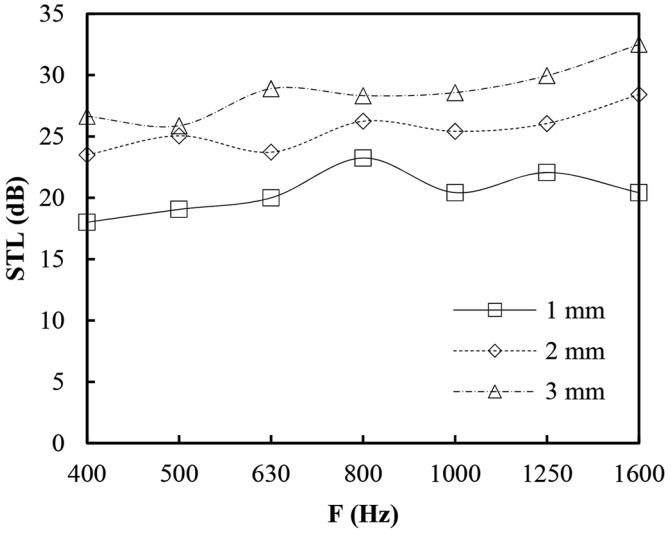

Fig. 7. Influence of material thickness on the normal incident STL for Ti6Al4V manufactured using SLM.

[66].

When it comes to α, a maximum difference of 0.06 was observed, which is a deviation of 6%. Generally, a 10 % variation in sound absorption coefficient equates to an uncertainty of 0.5 dB in the sound power absorbed which is also within the standard measurement uncertainty [67]. As such the impedance tube test rig developed in this study is accurate and can be used for characterising the acoustic performance of the material following relevant standards.

3.2. Sound absorption

The frequency-dependent normal incidence sound absorption coefficient for 3D printed Ti6Al4V and Ti6Al4V ELI samples are shown in Fig. 6a. Since α is a ratio of reflected to incident sound energy, a value of '0' indicates complete reflection without any absorption. On the other hand, a value of '1' indicates that all the sound energy is absorbed with no reflection. Consequently, for Ti6Al4V, an α curve representative of non-porous hard metals can be observed from Fig. 6. The highest absorption was observed at 500 Hz namely 0.15 and 0.14 for Ti6Al4V and Ti6Al4V ELI, respectively. This showed that approximately ~ 85–86 % of the sound energy is reflected without penetrating the surface of the material. While this shows both the Ti6Al4V and Ti6Al4V ELI

manufactured using SLM are fully dense from a structural point of view, the behaviour is acoustically poor and is similar to other dense hard metals such as steel.

When compared the performance between Ti6Al4V and Ti6Al4V ELI, the difference is negligible and are well within the measurement uncertainty. This means that the extra low interstitial version acoustically behaves like normal Ti6Al4V. Consequently, any further tests are limited to Ti6Al4V alone as the performance can be considered similar to Ti6Al4V ELI. The relatively high absorption at low frequencies (400–800 Hz) can be attributed to the 1 mm sample and the 44 mm air gap. This means that at low frequencies the sample can act as a baffle transferring the vibro-acoustic energy providing some damping. In any case, the difference between highest and lowest α values was limited to ~ 0.13 indicating an overall poor sound absorption of as manufactured SLM Ti6Al4V.

Fig. 6b shows the influence of material thickness on α for Ti6Al4V samples. A slight increase in α can be observed at the low frequencies which can be attributed to the shift in resonance frequency due to the added mass. The highest improvement of ~ 0.05 was found at the highest thickness of 3 mm at 630 Hz in comparison to 1 mm. While certain differences can be observed in the α peaks between the material thickness tested, overall sound absorption remained poor despite the increased material thickness. Nevertheless, the results establish that the overall accuracy of α depends on the material thickness and the variation in magnitude is higher at 500–800 Hz in comparison to other frequencies tested. Consequently, this study shows that SLM manufactured Ti6Al4V samples under optimum process parameters are fully dense and do not contribute significantly to sound absorption.

3.3. Sound transmission loss (STL)

While α is an important parameter determining the acoustic performance of the material, it is not the only one. Equally important is the sound transmission loss, which characterises the ability of a material to block sound. Sound-absorbing materials are generally porous and allow sound pressure fluctuations to enter their surface and dissipate energy through a variety of mechanisms. However, sound barrier materials reflect sound and are dense and nonporous. In general, a single homogeneous material will not be both a good absorber and a barrier.

Given the increasing application of Ti6Al4V as engine mounts and turbofans, it may be argued that the STL, in this case, is an important parameter than α. Accordingly, Fig. 7 shows the STL measured for Ti6Al4V samples featuring a thickness of 1, 2 and 3 mm. The results show that fully dense Ti6Al4V is excellent at resisting sound transmission and hence has a high STL. Generally, the higher the STL curve the better the acoustic isolation. This shows that Ti6Al4V is an ideal material to be used in noisy engines to deaden the sound.

Furthermore, the material thickness has a substantial impact on the STL curves. The highest rate of improvement (+5 dB *avg.*) was observed when the thickness was increased from 1 mm to 2 mm. Even though the performance further increased at 3 mm, the rate of improvement was limited to +3 dB *avg.* The improvement in STL due to thickness observed can be primarily attributed to the increase in mass and can be related using Eqn. (22):

$$STL_f \approx 20 \log 10\,(fm'') - 47 \tag{22}$$

where f is the frequency and m'' is the mass per unit area of the flat specimen. The mass law behaviour extends from the first resonance of the specimen up to just below the critical frequency. At high frequencies, the coincidence region occurs where the wavelengths in Ti6Al4V and air are similar. Here a dip in the STL occurs at the critical frequency; extended studies are needed to identify the extent of this dip and its dependence on the material.

3.4. Ti6Al4V micro-perforated panel

Traditional MPPs feature either circular or slit type [23] perforations that are distributed evenly along the panel face. The dimensions of which dictate the peak absorption frequency. However, having established the potential of using A_{perf} in the equivalent fluid model to design the MPP presented, the peak absorption was expected to occur at ~ 1000 Hz for all the three novel perforation shapes (M1, S1 and H1) following the Helmholtz theory.

Fig. 8 shows the α observed for the three micro-perforation designs considered. The micro-perforations have a significant impact on the performance with absorption improving for most of the frequencies (630–1600 Hz). However, a 10 % decrease in performance was observed at the lowest frequency (400–630 Hz) tested. While the performance of all the designs shows a similar trend, the best performance was exhibited by the design S1 followed by M1 and then H1.

The shape of perforation had a significant effect on the frequency of maximum α, only the design S1 (star-shaped perforation) corresponded with the theoretical frequency which can be attributed to the ratio of small to large perforation area (A_s/A_l). The designs S1, M1 and H1 featured a A_s/A_l values of 0.6, 0.3 and 0.15, respectively. Accordingly, it can be said that to use the perforation area instead of diameter in the equivalent fluid model, the ratio of perforations (A_s/A_l) has to be greater than 0.5. For the design H1 and M1, the peak absorption was observed at 1250 Hz as opposed to the design frequency of 1000 Hz. In addition, looking at the absorption values, the best performance was observed for design S1 again reiterating the importance of the A_s/A_l. The highest absorption despite sharing the same perforation area was observed for the highest A_s/A_l.

Even though the micro-perforations can be seen to improve the absorption, the best performances (25–30 % improvement) were observed at frequencies at or above 100 Hz. This is because of the inherent disadvantage demonstrated by the micro-perforation in suppressing the low-frequency noise (*i.e.* <1000 Hz) despite the optimal perforation area which is well documented [58]. To solve this problem, the layer interaction effect is exploited by coupling a 25 mm porous media to the highly stiff and reflective Ti6Al4V microperforated layer backed up by a 19 mm air cavity.

Fig. 9a shows the sound absorption of the 25 mm porous backed MPP featuring a 19 mm back cavity in comparison to the best performing Ti6Al4V MPP without a porous layer. It is clear from the results that the

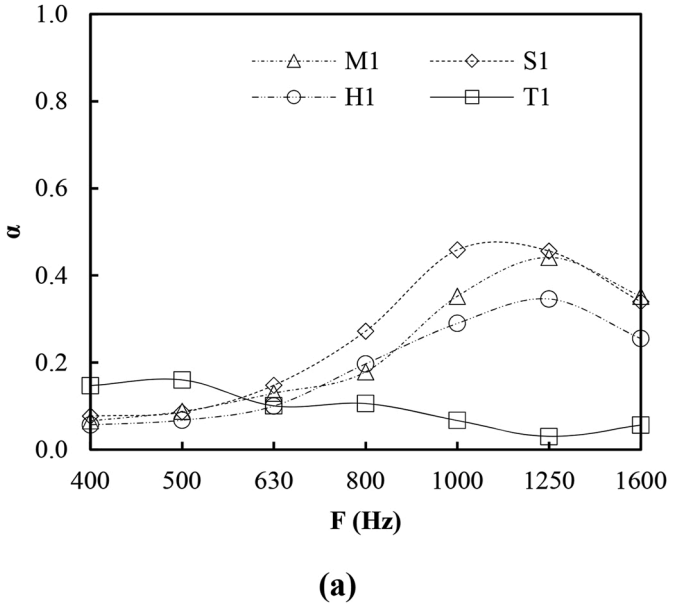

Fig. 8. The sound absorption of Ti6Al4V non-circular MPP designs with a 44 mm back cavity.

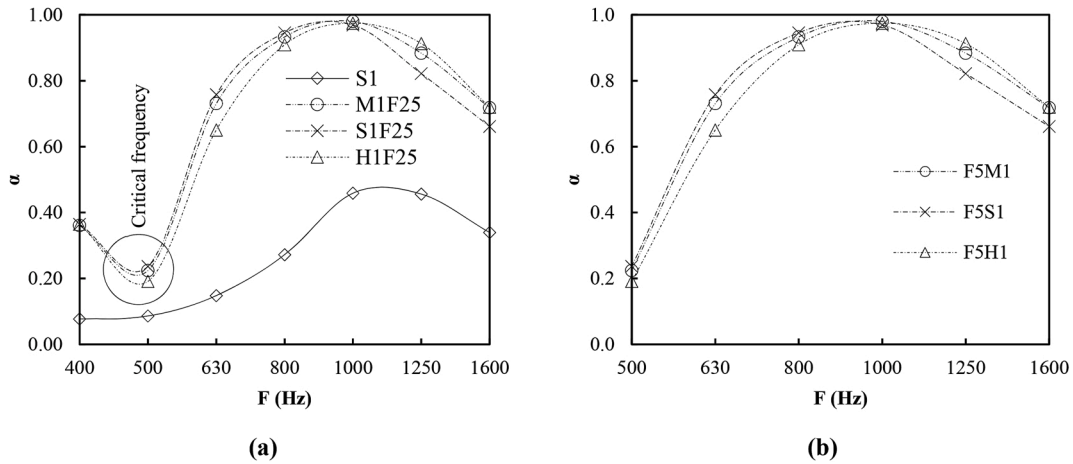

Fig. 9. The absorption coefficient observed for (a) micro-perforated Ti6Al4V panels featuring a 25 mm porous layer and (b) shows the results above the critical frequency for clarity.

addition of a porous layer significantly increases α in comparison to all other cases considered. The performance improvement can be primarily attributed to the interaction effect caused due to the constitutive parameters, importantly the ratio of porosity and stiffness between the MPP and porous medium. The contribution of the interaction effect to α is so significant that complete absorption was observed at a frequency range of 800–1250 Hz with the overall performance following a quadratic curve.

However, the improvement in α towards the lower frequency is limited by the critical frequency (f_c= 500 Hz) which is the first eigenmode frequency of the system. The critical frequency is identical for all F25 variants as they feature similar thicknesses. The critical frequency here is dependent on the stiffness of the panel, which is primarily influenced by the material thickness. Overall, the interaction effects of the hybrid system featuring both the MPP and the porous layer outperforms the case that of the MPP that feature only the back-cavity. The MPP by itself feature relatively large perforation and Ti6Al4V inherently possess high structural strength and reflectivity. The foam on the other hand offers a high porosity though it is structurally weak. However, the combination is acoustically effective for enhanced sound absorption (Fig. 9b). Furthermore, the MPPs demonstrate frequency dependency, which offers the potential for their sequential arrangement to enhance absorption at targeted frequencies. However, this aspect requires further experiments investigating the effect of multiple perforated panels arranged sequentially.

The manufacture of complex perforation in high strength metals such as Ti6Al4V, which can be coupled with a porous medium to develop high-efficiency sound absorbers in the low to medium frequency range is demonstrated in this paper. The study further validates that the perforations can be of any shape and not necessarily circular to obtain high α values when used with a porous layer. This allows the design to accommodate both structural strength and aesthetics when designing micro-perforations-based sound absorbers. Furthermore, a greater number of applications can be envisaged, both in room acoustics and industrial noise control.

4. Conclusion

Experimentally measured sound absorption coefficient (α) and transmission loss (STL) for additively manufactured Ti6Al4V specimens are presented in this study. The as-manufactured Ti6Al4V and Ti6Al4V ELI using optimum SLM parameters do not absorb sound well and exhibited a sound reflectivity of ~ 85–86 %. In addition, the α of Ti6Al4V and ELI variant was found to be similar with any differences less than the measurement uncertainty. While the influence of material thickness on the sound absorption was found to be insignificant (limited to 0.05_{α}), the highest material thickness (3 mm) exhibited the highest absorption (~ 0.18 *avg.*) along with the low frequencies (400–800 Hz). When it comes to STL, fully dense Ti6Al4V showed excellent performance with a +5 dB (*avg.*) increase on doubling the thickness. Nevertheless, the improvement in STL can be attributed primarily to the increase in mass following a trend that can be expressed as $20 \log 10\,(fm'') - 47$. The result of the novel Ti6Al4V MPP developed in this study shows significant improvement in α at all frequencies above the critical frequency (f_c) of 500 Hz. The high performance can be attributed to the interaction effect between the MPP and the porous layer. It was found that for non-circular perforation, the perforation area can be used for the equivalent fluid model to predict the peak absorption frequency. The development of traditional MPP has been limited due to their low absorption bandwidth at low frequency (<1000 Hz) and high manufacturing cost. These limitations can be overcome through AM allowing complex geometrically precise micro-perforation as demonstrated in this study.

Author statement

Arun Arjunan: Conceptualisation, Supervision, Methodology, Software, Investigation, Validation, Formal analysis, Writing original draft, Writing- Reviewing and Editing. Ahmad Baroutaji: Conceptualisation, Methodology, Software, Investigation, Validation, Formal analysis, Writing original draft, Writing- Reviewing and Editing. Ahmad Latif: Investigation, Formal analysis.

Declaration of competing interest

The authors declare that they have no known competing financial interests or personal relationships that could have appeared to influence the work reported in this paper.

Acknowledgements

This research was funded by the European Commission CALMERIC Grant 32R19P03053.

References

[1] P.M. Moradi, A. Kantzas, Visualization of acoustically-assisted fluid flow in unconsolidated confined porous media, Results Eng 6 (2020) 100114, https://doi.org/10.1016/j.rineng.2020.100114.
[2] Y. Jia, P. Xu, Noise cancellation in vibration signals using an oversampling and two-stage autocorrelation model, Results Eng 6 (2020) 100136, https://doi.org/10.1016/j.rineng.2020.100136.

[3] A.S. Praveen, A. Arjunan, Parametric optimisation of High-Velocity Oxy-Fuel Nickel-Chromium-Silicon-Boron and Aluminium-Oxide coating to improve erosion wear resistance, Mater. Res. Express (2019), https://doi.org/10.1088/2053-1591/ab301c.

[4] A. Rousounelos, S.J. Walsh, V.V. Krylov, J.L. Horner, Optimisation of the structural modes of automotive-type panels using line stiffeners and point masses to achieve weak acoustic radiation, Appl. Acoust. 93 (2015) 23–37, https://doi.org/10.1016/j.apacoust.2015.01.001.

[5] G. Chirico, G.N. Barakos, N. Bown, Propeller installation effects on turboprop aircraft acoustics, J. Sound Vib. 424 (2018) 238–262, https://doi.org/10.1016/j.jsv.2018.03.003.

[6] R. Flores, C. Asensio, P. Gagliardi, G. Licitra, Study of the correction factors for aircraft noise façade measurements, Appl. Acoust. 145 (2019) 399–407, https://doi.org/10.1016/j.apacoust.2018.10.007.

[7] A. Arjunan, C. Wang, M. English, M. Stanford, P. Lister, A computationally-efficient numerical model to characterize the noise behavior of metal-framed walls, Metals 5 (2015) 1414–1431, https://doi.org/10.3390/met5031414.

[8] A. Arjunan, C.J. Wang, K. Yahiaoui, D.J. Mynors, T. Morgan, V.B. Nguyen, M. English, Sound frequency dependent mesh modelling to simulate the acoustic insulation of stud based double-leaf walls. Proc. ISMA 2014 - Int. Conf. Noise Vib. Eng. USD 2014 - Int. Conf. Uncertain, Struct. Dyn., 2014.

[9] A. Arjunan, A. Baroutaji, A.S. Praveen, A.G. Olabi, C.J. Wang, Acoustic performance of metallic foams. Ref. Modul. Mater. Sci. Mater. Eng., Elsevier, 2019, https://doi.org/10.1016/B978-0-12-803581-8.11561-9.

[10] D.-Y. Maa, Potential of microperforated panel absorber, J. Acoust. Soc. Am. 104 (1998) 2861–2866, https://doi.org/10.1121/1.423870.

[11] D.-Y. Maa, Microperforated-panel wideband Absorbers, Noise Control Eng. J. 29 (1987) 77, https://doi.org/10.3397/1.2827694.

[12] H. Ruiz, P. Cobo, F. Jacobsen, Optimization of multiple-layer microperforated panels by simulated annealing, Appl. Acoust. 72 (2011) 772–776, https://doi.org/10.1016/j.apacoust.2011.04.010.

[13] J. Pfretzschner, P. Cobo, F. Simón, M. Cuesta, A. Fernández, Microperforated insertion units: an alternative strategy to design microperforated panels, Appl. Acoust. 67 (2006) 62–73, https://doi.org/10.1016/j.apacoust.2005.05.005.

[14] J. Kang, H.V. Fuchs, Predicting the absorption of open weave textiles and micro-perforated membranes backed by an air space, J. Sound Vib. 220 (1999) 905–920, https://doi.org/10.1006/jsvi.1998.1977.

[15] Q. Zhang, Y. Mao, D. Qi, Effect of perforation on the sound transmission through a double-walled cylindrical shell, J. Sound Vib. 410 (2017) 344–363, https://doi.org/10.1016/j.jsv.2017.08.041.

[16] X.-L. Gai, T. Xing, X.-H. Li, B. Zhang, Z.-N. Cai, F. Wang, Sound absorption properties of microperforated panel with membrane cell and mass blocks composite structure, Appl. Acoust. 137 (2018) 98–107, https://doi.org/10.1016/j.apacoust.2018.03.013.

[17] P. Cobo, M. Cuesta, Measuring hybrid passive-active sound absorption of a microperforated liner at oblique incidence, J. Acoust. Soc. Am. 125 (2009) 185–190, https://doi.org/10.1121/1.3026328.

[18] P. Cobo, M. Cuesta, Hybrid passive-active absorption of a microperforated panel in free field conditions, J. Acoust. Soc. Am. 121 (2007) EL251, https://doi.org/10.1121/1.2739112.

[19] P. Cobo, A. Fernández, Hybrid passive-active absorption of broadband noise using MPPs, Noise Vib. Worldw. 37 (2006) 19–23, https://doi.org/10.1260/095745606778600811.

[20] P. Cobo, F. Montero de Espinosa, Proposal of cheap microperforated panel absorbers manufactured by infiltration, Appl. Acoust. 74 (2013) 1069–1075, https://doi.org/10.1016/j.apacoust.2013.03.003.

[21] X.-L. Gai, T. Xing, Z.-N. Cai, F. Wang, X.-H. Li, B. Zhang, X.-W. Guan, Developing a Microperforated Panel with Ultra-micro Holes by Heat Shrinkable Materials, 2019, https://doi.org/10.1016/j.apacoust.2019.03.021.

[22] P. Cobo, J. Pfretzschner, M. Cuesta, D.K. Anthony, Hybrid passive–active absorption using microperforated panels, J. Acoust. Soc. Am. 116 (2004) 2118–2125, https://doi.org/10.1121/1.1786831.

[23] F. Auriemma, Acoustic performance of micro-grooved elements, Appl. Acoust. 122 (2017) 128–137, https://doi.org/10.1016/j.apacoust.2017.02.019.

[24] T.G. Zieliński, F. Chevillotte, E. Deckers, Sound absorption of plates with micro-slits backed with air cavities: analytical estimations, numerical calculations and experimental validations, Appl. Acoust. 146 (2019) 261–279, https://doi.org/10.1016/j.apacoust.2018.11.026.

[25] J.F. Ning, S.W. Ren, G.P. Zhao, Acoustic properties of micro-perforated panel absorber having arbitrary cross-sectional perforations, Appl. Acoust. 111 (2016) 135–142, https://doi.org/10.1016/j.apacoust.2016.04.012.

[26] H. Ruiz, P. Cobo, Sound absorption of single- and double-layer microperforated insertion units, J. Acoust. Soc. Am. 128 (2010), https://doi.org/10.1121/1.3508014, 2286–2286.

[27] T.J. Cox, P. D'Antonio, Acoustic Absorbers and Diffusers : Theory, Design and Application, Taylor & Francis, 2009.

[28] H. Meng, M.A. Galland, M. Ichchou, F.X. Xin, T.J. Lu, On the low frequency acoustic properties of novel multifunctional honeycomb sandwich panels with micro-perforated faceplates, Appl. Acoust. 152 (2019) 31–40, https://doi.org/10.1016/j.apacoust.2019.02.028.

[29] H. Min, W. Guo, Sound absorbers with a micro-perforated panel backed by an array of parallel-arranged sub-cavities at different depths, Appl. Acoust. 149 (2019) 123–128, https://doi.org/10.1016/j.apacoust.2019.01.013.

[30] I.M. Miasa, M. Okuma, G. Kishimoto, T. Nakahara, An experimental study of a multi-size microperforated panel absorber, J. Syst. Des. Dyn. 1 (2007) 331–339, https://doi.org/10.1299/jsdd.1.331.

[31] A.I. Mosa, A. Putra, R. Ramlan, I. Prasetiyo, A.-A. Esraa, Theoretical model of absorption coefficient of an inhomogeneous MPP absorber with multi-cavity depths, Appl. Acoust. 146 (2019) 409–419, https://doi.org/10.1016/j.apacoust.2018.11.002.

[32] M.A. Temiz, J. Tournadre, I.L. Arteaga, A. Hirschberg, Non-linear acoustic transfer impedance of micro-perforated plates with circular orifices, J. Sound Vib. 366 (2016) 418–428, https://doi.org/10.1016/j.jsv.2015.12.022.

[33] M.A. Temiz, J. Tournadre, I. Lopez Arteaga, A. Hirschberg, Modelling vibro-acoustic coupling in flexible micro-perforated plates by a patch-impedance approach, Appl. Acoust. 125 (2017) 80–90, https://doi.org/10.1016/j.apacoust.2017.04.012.

[34] H.-S. Kim, P.-S. Ma, S.-R. Kim, S.-H. Lee, Y.-H. Seo, A model for the sound absorption coefficient of multi-layered elastic micro-perforated plates, J. Sound Vib. 430 (2018) 75–92, https://doi.org/10.1016/j.jsv.2018.05.036.

[35] S. Greiner, K. Wudy, L. Lanzl, D. Drummer, Selective laser sintering of polymer blends: bulk properties and process behavior, Polym. Test. 64 (2017) 136–144, https://doi.org/10.1016/j.polymertesting.2017.09.039.

[36] J. Robinson, M. Stanford, A. Arjunan, Stable formation of powder bed laser fused 99.9% silver, Mater. Today Commun (2020) 101195, https://doi.org/10.1016/j.mtcomm.2020.101195.

[37] A. Arjunan, Acoustic absorption of passive destructive interference cavities, Mater. Today Commun. 19 (2019) 68–75, https://doi.org/10.1016/j.mtcomm.2018.12.012.

[38] A. Arjunan, Targeted sound attenuation capacity of 3D printed noise cancelling waveguides, Appl. Acoust. 151 (2019) 30–44, https://doi.org/10.1016/j.apacoust.2019.03.008.

[39] T.C. Dzogbewu, Laser powder bed fusion of Ti15Mo, Results Eng 7 (2020) 100155, https://doi.org/10.1016/j.rineng.2020.100155.

[40] X.H. Zhang, Z.G. Qu, X.C. He, D.L. Lu, Experimental study on the sound absorption characteristics of continuously graded phononic crystals, AIP Adv. 6 (2016) 105205, https://doi.org/10.1063/1.4965923.

[41] N. Gao, H. Hou, Sound absorption characteristic of micro-helix metamaterial by 3D printing, Theor. Appl. Mech. Lett. 8 (2018) 63–67, https://doi.org/10.1016/j.taml.2018.02.001.

[42] R. Aslan, O. Turan, Gypsum-based sound absorber produced by 3D printing technology, Appl. Acoust. 161 (2020) 107162, https://doi.org/10.1016/j.apacoust.2019.107162.

[43] A. Arjunan, A. Baroutaji, J. Robinson, Advances in acoustic metamaterials. Ref. Modul. Mater. Sci. Mater. Eng., Elsevier, 2021, https://doi.org/10.1016/B978-0-12-815732-9.00091-7.

[44] N. Yang, Novel structural design method inspired by DNA and origami, Results Eng 4 (2019) 100069, https://doi.org/10.1016/j.rineng.2019.100069.

[45] A. Albar, M. Chougan, M.J. Al- Kheetan, M.R. Swash, S.H. Ghaffar, Effective extrusion-based 3D printing system design for cementitious-based materials, Results Eng 6 (2020) 100135, https://doi.org/10.1016/j.rineng.2020.100135.

[46] A. Arjunan, A. Baroutaji, J. Robinson, C. Wang, Characteristics of acoustic metamaterials. Ref. Modul. Mater. Sci. Mater. Eng., Elsevier, 2021, https://doi.org/10.1016/B978-0-12-815732-9.00090-5.

[47] Y. Wu, M. Yang, P. Sheng, Perspective: acoustic metamaterials in transition, J. Appl. Phys. (2018), https://doi.org/10.1063/1.5007682.

[48] L.T. Govindaraman, A. Arjunan, A. Baroutaji, J. Robinson, A.-G. Olabi, Metamaterials for energy harvesting. Ref. Modul. Mater. Sci. Mater. Eng., Elsevier, 2021, https://doi.org/10.1016/B978-0-12-815732-9.00127-3.

[49] A. Arjunan, M. Singh, A. Baroutaji, C. Wang, Additively manufactured AlSi10Mg inherently stable thin and thick-walled lattice with negative Poisson's ratio, Compos. Struct. 247 (2020) 112469, https://doi.org/10.1016/j.compstruct.2020.112469.

[50] V. Amaya-Amaya, M. de Icaza-Herrera, A.L. Martínez-Hernández, G. Martínez-Barrera, C. Velasco-Santos, Experimental approximation of the sound absorption coefficient (∝) for 3D printed reentrant auxetic structures of poly lactic acid reinforced with chicken keratin materials, Mater. Lett. 283 (2021) 128757, https://doi.org/10.1016/j.matlet.2020.128757.

[51] R. Tayong, T. Dupont, P. Leclaire, Experimental investigation of holes interaction effect on the sound absorption coefficient of micro-perforated panels under high and medium sound levels, Appl. Acoust. 72 (2011) 777–784, https://doi.org/10.1016/j.apacoust.2011.04.011.

[52] N. Atalla, F. Sgard, Modeling of perforated plates and screens using rigid frame porous models, J. Sound Vib. 303 (2007) 195–208, https://doi.org/10.1016/j.jsv.2007.01.012.

[53] U. Ingard, On the theory and design of acoustic resonators, J. Acoust. Soc. Am. 25 (1953) 1037–1061, https://doi.org/10.1121/1.1907235.

[54] Y.J. Qian, D.Y. Kong, S.M. Liu, S.M. Sun, Z. Zhao, Investigation on micro-perforated panel absorber with ultra-micro perforations, Appl. Acoust. 74 (2013) 931–935, https://doi.org/10.1016/j.apacoust.2013.01.009.

[55] R.L. Panton, J.M. Miller, Resonant frequencies of cylindrical Helmholtz resonators, J. Acoust. Soc. Am. 57 (1975) 1533–1535, https://doi.org/10.1121/1.380596.

[56] C. Cai, C.M. Mak, Noise control zone for a periodic ducted Helmholtz resonator system, J. Acoust. Soc. Am. 140 (2016) EL471–EL477, https://doi.org/10.1121/1.4968530.

[57] S. Kim, Y.-H. Kim, J.-H. Jang, A theoretical model to predict the low-frequency sound absorption of a Helmholtz resonator array (L), J. Acoust. Soc. Am. 119 (2006) 1933–1936, https://doi.org/10.1121/1.2177568.

[58] S.-H. Park, Acoustic properties of micro-perforated panel absorbers backed by Helmholtz resonators for the improvement of low-frequency sound absorption, J. Sound Vib. 332 (2013) 4895–4911, https://doi.org/10.1016/j.jsv.2013.04.029.

[59] K.U. Ingard, Notes on Sound Absorption Technology, Noise Control Foundation, 1994.
[60] M. Bisht, N. Ray, F. Verbist, S. Coeck, Correlation of selective laser melting-melt pool events with the tensile properties of Ti-6Al-4V ELI processed by laser powder bed fusion, Addit. Manuf. 22 (2018) 302–306, https://doi.org/10.1016/J.ADDMA.2018.05.004.
[61] Y. Zhai, H. Galarraga, D.A. Lados, Microstructure, static properties, and fatigue crack growth mechanisms in Ti-6Al-4V fabricated by additive manufacturing: LENS and EBM, Eng. Fail. Anal. 69 (2016) 3–14, https://doi.org/10.1016/j.engfailanal.2016.05.036.
[62] K. Bari, A. Arjunan, Extra low interstitial titanium based fully porous morphological bone scaffolds manufactured using selective laser melting, J. Mech. Behav. Biomed. Mater. 95 (2019) 1–12, https://doi.org/10.1016/j.jmbbm.2019.03.025.
[63] A. Vance, K. Bari, A. Arjunan, Investigation of Ti64 sheathed cellular anatomical structure as a tibia implant. https://doi.org/10.1088/2057–1976/ab0bd7, 2019, 5.
[64] ISO10534, Acoustics – Determination of Sound Absorption Coefficient and Impedance in Impedance Tubes – Part 2: Transfer-Function Method, 1998.
[65] BS, 2001. ENISO10534-2, Determination of Sound Absorption Coefficient and Impedance in Impedance Tubes, Part 2: Transfer-Function Method, British Standards Organisation, 2001.
[66] BSENISO10140-1, Acoustics, Laboratory Measurement of Sound Insulation of Building Elements. Application Rules for Specific Products, British Standards Organisation, 2016.
[67] J. Han, D.W. Herrin, A.F. Seybert, Accurate measurement of small absorption coefficients, SAE Tech. Pap. (2007), https://doi.org/10.4271/2007-01-2224.